

AD A110609

DTIC FILE COPY

~~76-7642~~  
LEVEL

①

<sup>6</sup> CHARACTERIZATION OF ELECTRICALLY ACTIVE  
DEFECTS IN Si USING CCD IMAGE SENSORS

<sup>10</sup> H. F. Schaaake  
W. C. Rhines

Texas Instruments Incorporated

11 October 1976

<sup>9</sup> Quarterly Technical Report  
30 July 1976 - 31 October 1976

APPROVED FOR PUBLIC RELEASE  
DISTRIBUTION UNLIMITED

Sponsored by  
Advanced Research Projects Agency

N00173-76-C-0280, ARPA Order No. 3219

The views and conclusions contained in this document are those of the authors and should not be interpreted as necessarily representing the official policies, either expressed or implied, of the Advanced Research Projects Agency or the U. S. Government.

ES  
ROU  
82 02 05 053  
403833

DTIC  
RECEIVED  
FEB 8 1982  
H

(12)

QUARTERLY TECHNICAL REPORT  
CONTRACT NO. N00173-76-C-0280  
30 July 1976 - 31 October 1976

ARPA Order-3219

Sponsored by  
Advanced Research Projects Agency  
ARPA Order No. 3219

DTIC  
FEB 8 1982  
H

ARPA Order Number: 3219  
Program Code Number: 6D10

Name of Contractor: Texas Instruments Incorporated  
Central Research Laboratories  
P. O. Box 5936  
Dallas, Texas 75222

Effective Date of Contract: 30 July 1976

Contract Expiration Date: 30 March 1978

Amount of Contract: \$205,329.00

Contract Number: N00173-76-C-0280

Principal Investigator and Phone No. : Dr. H. F. Schaake  
(214) 238-4204

Scientific Officer and Phone No. : Dr. Dave Barbe - Code 5260  
Naval Research Laboratory  
(202) 767-2408

Short Title of Work: Characterization of Electrically Active  
Defects in Si Using CCD Image Sensors

The views and conclusions contained in this document are those of the authors and should not be interpreted as necessarily representing the official policies, either expressed or implied, of the Advanced Research Projects Agency or the U. S. Government.

APPROVED FOR PUBLIC RELEASE  
DISTRIBUTION UNLIMITED

## TABLE OF CONTENTS

<u>SECTION</u>		<u>PAGE</u>
I	INTRODUCTION. . . . .	1
II	TECHNICAL APPROACH. . . . .	2
	A. X-ray Topography. . . . .	2
	B. Transmission Electron Microscopy. . . . .	21
III	EXPERIMENTAL RESULTS. . . . .	23
	A. X-ray Topography. . . . .	23
	B. Transmission Electron Microscopy. . . . .	23
	C. Electrical Device Fabrication . . . . .	27
IV	FUTURE RESEARCH . . . . .	35
	A. X-ray Topography. . . . .	35
	B. Transmission Electron Microscopy. . . . .	35
	C. Device Fabrication and Testing. . . . .	35
	REFERENCES. . . . .	36

## LIST OF ILLUSTRATIONS

<u>FIGURE</u>		<u>PAGE</u>
1	Transmission X-ray Topography . . . . .	3
2(a)	Film Contrast Sensitivity versus Exposure for $\text{MoK}\alpha_1$ Radiation . . . . .	13
2(b)	Film Contrast Sensitivity versus Exposure for $\text{CuK}\alpha_1$ Radiation . . . . .	14
3	Silicon Bar Etched in 3 Parts $\text{HNO}_3$ to 1 Part HF . . . . .	26
4	Device Number Positions on 7.6 cm Slices. . . . .	32

## LIST OF TABLES

<u>TABLE</u>		<u>PAGE</u>
1	Structure Factor of Silicon . . . . .	6
2	Relative Sensitivity of Reflections to Detecting Defects (Constant Exposure Time). . . . .	18
3	Relative Sensitivity of Reflections to Detecting Defects (Constant Exposure) . . . . .	19



(12)

QUARTERLY TECHNICAL REPORT  
CONTRACT NO. N00173-76-C-0280  
30 July 1976 - 31 October 1976

ARPA Order-3219

Sponsored by  
Advanced Research Projects Agency  
ARPA Order No. 3219

DTIC  
FEB 8 1982  
H

ARPA Order Number: 3219  
Program Code Number: 6D10

Name of Contractor: Texas Instruments Incorporated  
Central Research Laboratories  
P. O. Box 5936  
Dallas, Texas 75222

Effective Date of Contract: 30 July 1976

Contract Expiration Date: 30 March 1978

Amount of Contract: \$205,329.00

Contract Number: N00173-76-C-0280

Principal Investigator and Phone No. : Dr. H. F. Schaake  
(214) 238-4204

Scientific Officer and Phone No. : Dr. Dave Barbe - Code 5260  
Naval Research Laboratory  
(202) 767-2408

Short Title of Work: Characterization of Electrically Active  
Defects in Si Using CCD Image Sensors

The views and conclusions contained in this document are those of the authors and should not be interpreted as necessarily representing the official policies, either expressed or implied, of the Advanced Research Projects Agency or the U. S. Government.

APPROVED FOR PUBLIC RELEASE  
DISTRIBUTION UNLIMITED

### TECHNICAL REPORT SUMMARY

The purpose of this project is to determine the nature and origin of defects that produce dark-current spikes in CCD area imagers.

During this quarter, silicon wafers of various crystallographic orientations, and with established identity with respect to the boules from which they were grown, were obtained. Processing of the first lot of devices has commenced, as has structural characterization of the starting material.

Two technical problems pertaining to structural characterization techniques have been treated in some detail. Their solution will result in a significant increase in the quality and quantity of data obtained during the course of this investigation.

X-ray topography has been examined from a theoretical standpoint to determine the operating conditions that will result in maximum sensitivity to various types of structural defects. It has been determined that certain reflections are clearly superior. These will be used during the course of the investigation. Experimental confirmation of these findings has been obtained for the case of a (111) wafer. In addition, it has been determined that a significant increase in the sensitivity of x-ray topography to the detection of defects may be obtained by greatly increasing exposure time. An investigation of film developers capable of dealing with the prolonged exposures is under way.

A multistep technique to thin a selected region of a CCD area imager that contains a dark-current defect to a thickness of  $\sim 5000$  Å required for transmission electron microscopy has been devised and is under development. The procedure consists of grinding the sample to  $\sim 100$   $\mu\text{m}$  thickness while maintaining the ground surface parallel to the device surface to within 5  $\mu\text{m}$ , an initial etch to  $\sim 15$   $\mu\text{m}$  thickness, etching out a 2.3 mm diameter disc

containing the defect for the electron microscope using a photoresist etch mask, final etching to 1/2 to 2  $\mu\text{m}$  thickness, and ion milling to obtain the desired thickness in the defect region of the disc. The grinding and etching steps are under control, and suitable etches have been found. Work is under way in thinning reject CCV area imagers to perfect the technique.

Preliminary studies of dark current were performed to ascertain effects that could be attributed to starting material and backside damage. For these tests, CCD imagers were fabricated on material of several different types of silicon substrates. The results clearly showed that the dark current was significantly higher for devices fabricated on some wafers than on others. There were also clear indications that the dark current on devices fabricated on float-zone material was significantly higher than that of devices fabricated on Czochralski material, and that the application of backside damage to the starting material had a beneficial effect in reducing device dark current.

With the controlled material that has been obtained, it should be possible to determine the reason for the wafer-to-wafer variations that have been observed. In addition, the role of backside wafer damage in reducing dark current should become clearer. The application of the techniques developed for x-ray topography and electron microscopy to the dark current in devices fabricated on this material should determine the causes of dark current in CCD area imagers.

## SECTION I

### INTRODUCTION

The detection and structural characterization of defects that cause dark-current blemishes in CCD array imagers is of central importance to the current investigation. Two structural characterization techniques are being used: x-ray topography and transmission electron microscopy. In reviewing the state of each of these techniques, it has become apparent that significant improvements could be made to greatly enhance the quantity and quality of data that can be obtained in the current investigation.

The inherent limitations in the use of x-ray topography to characterize defects lie in the sensitivity of the technique to the detection of small defects. Specifically, the question arises as to which reflections, exposures, films, etc., should be used to maximize the sensitivity of the technique to the detection of these defects. This area has never been fully treated in the literature. The discussion of this subject in Section II of this report shows that it should be possible to make significant improvements in the detectability of these defects.

The inherent limitation in electron microscopy is in the sample preparation stage; that is, in thinning the sample so that the defect is in a region no more than  $\sim 5000 \text{ \AA}$  thick. Work is under way to develop improved and reliable techniques of sample thinning so that an isolated defect will occur in such a region.

During the past quarter, material has been ordered and obtained for a series of experiments using controlled material parameters. Details of this material are reported in Section III. Processing on the first lot of CCD area imagers has commenced using a  $> 80 \text{ K bit}$ , two-phase device.

In addition, survey tests have been conducted on the dark current produced in devices made on a variety of different starting materials. Results of these experiments are also reported in Section III.

## SECTION II

### TECHNICAL APPROACH

#### A. X-Ray Topography

It is convenient to divide x-ray topography into three distinct areas: x-ray optics, which are determined by the geometric characteristics of the x-ray source and camera; contrast-forming mechanisms, which are determined by the nature of the defect and the diffraction conditions used; and the photographic exposure and development process. Together, these three areas will determine the sensitivity of the resulting topograph to the detection of defects in the sample. The subject of x-ray optics in topography has received abundant attention in the literature. Diffraction-contrast theory has received moderate attention, most notably for effects requiring the dynamical theory for explanation. The role of the photographic process has been largely ignored in x-ray topography, although there is a large body of information in the photographic literature that bears directly on this topic. In the following discussion we shall review or develop the theory in each of these areas as it pertains to the sensitivity of x-ray topography to the detection of defects. We shall then combine these results to determine the optimum operating conditions.

##### 1. X-Ray Optics

The arrangement for transmission x-ray topography is illustrated in Figure 1. In this figure we are looking down on the apparatus. The slits closest to the x-ray source limit the horizontal divergence of the x-ray beam so that only the  $K\alpha_1$  component is diffracted by the sample. The second set of slits prevents the main beam from falling on the film, allowing only the diffracted beam to expose the film. Since the first set of slits defines a line of x-rays normal to the figure, the film and sample are scanned through this beam to form an image on the film of the diffracted x-ray intensity from the entire sample. Reflection topography is similar, except that the diffracted beam emerges from the same side of the sample as the incident beam. Since the main beam now passes through the sample, the second set of slits is not needed and is usually omitted.



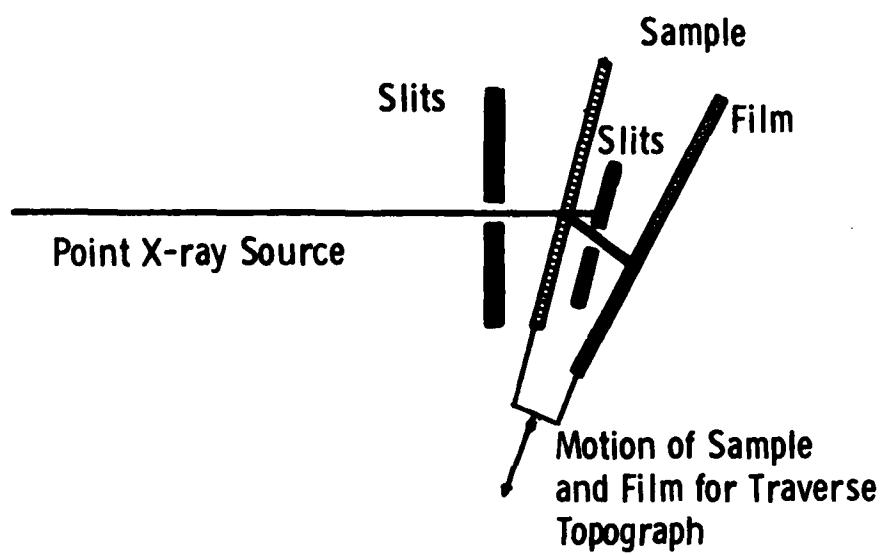


Figure 1 Transmission X-ray Topography

The optical resolution is of primary importance in determining the sensitivity of topography to defects. To determine the resolution, we consider a point on the sample and determine how it will be projected on the film by the diffraction process. Considering first the plane of Figure 1, we note the resolution is controlled by the diffraction width of the peak. For a purely monochromatic beam, the sample will diffract over  $\sim 3$  seconds arc. The x-ray source, however, has a wavelength dispersion that causes diffraction over 5 to 60 seconds arc and, hence, determines the resolution in this plane. For transmission topography, the necessity of the second slits limits the sample-to-film distance to  $\sim 1$  cm. This means that the horizontal resolution is  $\geq 1 \mu\text{m}$ . In reflection topography the sample-film distance can be  $< 0.5$  cm. However, since reflection topography requires working at higher diffraction angles, the effect of wavelength dispersion is greater, limiting us again to  $\sim 1 \mu\text{m}$  resolution.

The resolution in the plane normal to Figure 1 is determined by the x-ray source spot size, source-to-sample distance, and sample-to-film distance in the following manner:

$$R = \frac{dS}{L},$$

where  $d$  is the film-sample distance,  $S$  the spot size, and  $L$  the sample-spot distance. In our Automated Topography System<sup>1</sup> the spot size is typically  $200 \mu\text{m}$ , and the spot-sample distance is  $100$  cm. Thus, the vertical resolution is from  $1$  to  $2 \mu\text{m}$ . Because the sample-film distance can be less in reflection topography than in transmission, the resolution can be greater in reflection topography.

Three additional sources can cause loss of resolution: misorientation of the film, tilting of the translation stage during translation, and vibrations. Film misorientation can be a problem because thick emulsions ( $25$  to  $50 \mu\text{m}$ ) are

used. If a 50  $\mu\text{m}$  emulsion is misoriented  $1^\circ$  from the perpendicular to the diffracted beam, the resulting image will be broadened by 1  $\mu\text{m}$  when viewed by perpendicular light. This error can be corrected by changing the angle of viewing illumination, however. The effects of the other two sources have been minimized in the design of our Automated Topography System.

When the effects of all resolution degraders is taken into consideration, we find that the best resolution that can be readily obtained is  $\sim 1 \mu\text{m}$ ; i.e., a point would be broadened to a circle 1  $\mu\text{m}$  in diameter under optimum conditions. This is most readily obtained in the reflection mode.

## 2. Contrast Mechanisms

While there is considerable interest in the calculation of the diffraction images obtained in x-ray topography,<sup>2-6</sup> the exact solutions used by these techniques can be treated only numerically. We shall therefore consider the contrast problem in a semiquantitative manner similar to Authier<sup>7</sup> and Meier.<sup>8</sup>

The integrated intensity diffracted by a perfect, nonabsorbing crystal is given by<sup>9</sup>

$$\rho = \frac{8}{3\pi} \frac{\lambda^2}{\sin 2\theta_0} \frac{|F(h)|}{V} r_e \sqrt{\frac{\gamma_h}{\gamma_0}} \frac{1 + |\cos 2\theta_0|}{2},$$

where  $\lambda$  is the wavelength of radiation;  
 $\theta_0$  the Bragg angle;  
 $|F(h)|$  the structure factor, tabulated for silicon in Table I;  
 $V$  the unit cell volume;  
 $r_e$  the classical electron radius ( $= 2.82 \times 10^{-13}$  cm);  
 $\gamma_h$  the cosine of the angle between the diffracted beam direction and the normal to the crystal surface; and

Table 1  
Structure Factor of Silicon

<u>(hkl)</u>	<u>  F(h)  </u>
111	43
220	71
311	33
400	62
331	29
422	54
511	26
333	26
440	48

$\gamma_0$  the cosine of the angle between the incident beam direct and the normal to the crystal surface.

The angular width over which the crystal will diffract is given by

$$\Delta\gamma = \frac{2 |C| r_e \lambda^2}{\pi} \frac{|F(h)|}{V} \sqrt{\frac{\gamma_h}{\gamma_0}},$$

where  $|C|$  is a polarization term equal to 1 or  $\cos 2\theta_0$ , depending on the polarization of the incident radiation.

Now if a defect is present, a portion of the distorted volume surrounding the defect will diffract kinematically according to<sup>10</sup>:

$$\rho = \frac{\lambda^3 |F(h)|^2}{\sin 2\theta_0 v^2} r_e^2 \frac{1 + \cos^2 2\theta_0}{2} \Delta v,$$

where  $v$  is the diffracting volume. Authier<sup>7</sup> has experimentally determined that the material surrounding the defect whose diffracting planes are tilted more than  $x\Delta\gamma$ , where  $x$  is a number between 1 and 2, will diffract kinematically. The tilting of the planes surrounding a defect has also been determined by Authier<sup>11</sup>:

$$\delta = - \frac{1}{\cos \theta_0} \frac{\partial(\hat{s}_h \cdot \vec{u})}{\partial s_h},$$

where  $\hat{s}_h$  is the unit normal to the diffracting planes, and  $\vec{u}$  is the displacement field of the defect. We shall consider three types of displacement fields:

$$u_1 = M \tan^{-1} \frac{y}{x}$$

$$u_2 = M/r$$

and  $u_3 = M/2r^2$

The first of these is typical of a dislocation, the second the displacement field of an infinitely long dislocation dipole, and the third the displacement field of a small dislocation loop in the asymptotic limit or a precipitate particle. Substituting these into the previous equations, we find for  $u_n$

$$|\delta| = \left| \frac{M}{r^n \cos \theta_0} \right|,$$

if  $|\delta| = x\Delta\psi$ , the image size will be given by

$$L = 2 \left( \frac{M\pi V}{2 |C| r_e \lambda^2 |F(h)| \cos \theta_0} \times \sqrt{\frac{\gamma_0}{\gamma_n}} \right)^{1/n}.$$

The ratio of the intensity diffracted by the defect to the background perfect crystal intensity will be the contrast. Within the defect image, this will be

$$\frac{\Delta I}{I_0} \propto \lambda^{(1 - 2/n)} F(h)^{1 - 1/n} \left( \frac{\gamma_0}{\gamma_n} \right)^{\left( \frac{1}{2} + \frac{1}{2n} \right)},$$

where we have retained only experimentally variable terms and neglected less important trigonometric terms.

So far, we have neglected the effect of absorption. In the transmission case, the kinematical image will be attenuated by a factor  $\exp(-\mu t)$ , where  $\mu$  is the linear absorption coefficient, and  $t$  is the thickness of the sample. The perfect crystal diffracted intensity will also decrease, but not nearly so strongly. Therefore, in transmission topography we need to keep  $\mu t < 1$  to maximize kinematical contrast. In reflection



topography the kinematical image of a defect lying a distance  $t$  below the surface will be attenuated by a factor  $\exp\left[-\mu\left(\frac{1}{Y_0} + \frac{1}{Y_h}\right)t\right]$ , while the perfect crystal diffracted intensity is affected little. For example with  $\text{CuK}\alpha_1$  radiation and a (422) reflection from a (100) slice, the image intensity of a defect lying  $5\text{ }\mu\text{m}$  below the surface will be reduced by 44%, while that of a defect lying  $20\text{ }\mu\text{m}$  below the surface will be reduced 90% over that of a defect at the surface. Reflection topography is therefore a method for imaging near-surface defects.

We have also ignored the effect of temperature. This can be rectified by replacing  $|F(h)|$  with  $|F(h)| \exp[-M(h)]$ , where  $M(h)$  is the Debye-Waller factor.<sup>12</sup> Lattice vibrations will cause a reduction in the structure factor, with strongest effects for high (hkl).<sup>10</sup> We shall, however, continue to ignore the effect of temperature.

In addition to the kinematical contrast considered thus far, there are changes in the perfect crystal diffraction properties in the neighborhood of a defect that may affect contrast in transmission topographs. Since these effects are complex and generally contribute much less intensity to the image than do kinematical effects, they will not be considered here.

### 3. Photographic Processes

The x-ray intensity pattern determined by the optics and contrast mechanism falls on the film, thereby exposing grains. The developed film yields the image from which we detect the presence of the defect. In order for the defect to be detectable, the number of grains exposed by the defect image,  $\Delta N$ , must be greater than the statistical fluctuations of the background intensity,  $N$ . In other words, a defect is detectable when

$$\frac{\Delta N}{\sqrt{N}} > J ,$$

where  $J$  is some number ( $= 2$  for detectability at the 95% confidence limits).

To relate the above quantity to the x-ray intensity coming from the crystal, it is necessary to consider the exposure process. It is well established that an x-ray quantum, in the energy range with which we are dealing, is absorbed in a single grain, rendering it highly exposed.<sup>13</sup> This means that probability for the development of the grain is essentially unity. We may therefore determine the probability  $P(x)$  that a grain lying at depth  $x$  below the surface of the photographic emulsion will have been exposed at time  $t$ . This we can calculate by considering the probability  $dP(x)$  that the grain will be exposed at time  $t$ , which is simply the probability that the grain will absorb a quanta times the probability that the grain has not been exposed:

$$dP(x) = I(x)A_g[1 - \exp(-\mu d)][1 - P(x)] dt.$$

Here,  $I(x)$  is the x-ray intensity at a depth  $x$  below the surface,  
 $A_g$  is the area of the grain in the x-ray beam,  
 $\mu$  is the linear absorption coefficient of the grain, and  
 $d$  is the thickness of the grain.

For small  $d$  we note

$$A_g[1 - \exp(-\mu d)] \approx \mu A_g d = \mu V_g ,$$

where  $V_g$  is the grain volume.

We solve for  $P(x)$ :

$$P(x) = 1 - \exp[-\mu V_g I(x)t].$$

Now  $I(x)t$  is the exposure the grain will have received through time  $t$ ,  $E(x)$ . Also, we note

$$E(x) = E_0 \exp(-\mu_0 x) ,$$

where  $\mu_0$  is the linear absorption coefficient of the emulsion and is related to the linear absorption coefficient of the grain by

$$\mu_0 = \phi \mu ,$$

where  $\phi$  is the packing density of the halide grains; that is, the volume ratio of silver halide to the total emulsion volume. The number of grains at depth between  $x$  and  $x + dx$  and in an area  $A$  of the x-ray beam is

$$n = \frac{\phi A}{V_g} dx .$$

Hence, the number of grains exposed at this depth will be

$$dN = \frac{\phi A}{V_g} [1 - \exp(-\mu V_g E_0 \exp(-\mu_0 x))] dx .$$

The total number of exposed grains is obtained by integrating over the thickness of the emulsion

$$N = \frac{\phi A}{V_g} \int_0^t [1 - \exp(-\mu V_g E_0 \exp(-\mu_0 x))] dx .$$

The integration may be performed by expanding the first exponent in a power series. The result is

$$N = \frac{A}{V_g \mu_0} \left[ \sum_{n=1}^{\infty} \frac{(-\mu V_g E_0)^n [\exp(-n \mu_0 t) - 1]}{n \cdot n!} \right]$$

We can solve for  $\Delta N$  in terms of  $\Delta E_0$  by differentiating  $dN$  with respect to  $E_0$  before integrating:

$$d(\Delta N) = \mu_0 A \Delta E_0 \exp(-\mu_0 x) \exp[-\mu V_g E_0 \exp(-\mu_0 x)] dx ,$$

which may be integrated to give

$$\Delta N = \frac{\phi A}{V_g \mu_o} \frac{\Delta E}{E_o} \left\{ \exp[-\mu V_g E_o \exp(-\mu_o t)] - \exp(-\mu V_g E_o) \right\},$$

yielding, finally,

$$\frac{\Delta N}{\sqrt{N}} = \frac{\Delta E}{E_o} \sqrt{\frac{\phi A}{V_g \mu_o}} \left\{ \frac{\exp[-\mu V_g E_o \exp(-\mu_o t)] - \exp(-\mu V_g E_o)}{\sum_{n=1}^{\infty} \frac{(-\mu V_g E_o)^n [\exp(-n \mu_o t) - 1]}{n \cdot n!}} \right\}^{1/2}.$$

In the limit when the probability of the exposure of any grain is small, i.e.,  $\mu V_g E_o \ll 1$ , the above equation simplifies to:

$$\frac{\Delta N}{\sqrt{N}} = \frac{\Delta E}{E_o} \left\{ E_o A [1 - \exp(-\mu_o t)] \right\}^{1/2}.$$

In Figure 2 we have plotted  $[(E/E_o) \sqrt{A}]$  versus  $E_o$  for various nuclear emulsions under the assumption that  $\frac{\Delta N}{\sqrt{N}} = 2$ . For these curves the linear absorption coefficient  $\mu_o$  was measured, the packing density was assumed to be 0.5, and the manufacturer's stated mean grain sizes ( $0.13 \mu\text{m}$  for L-4,  $0.32 \mu\text{m}$  for G-5) were used. An arrow is also indicated for typical exposure when the plate is developed in Kodak D-19 developer.

These curves illustrate several interesting points.

(1) At the exposures typically used, the detection of small defects is clearly noise-limited. For example, a  $9 \mu\text{m}^2$  defect would have to give rise to an intensity difference of at least 20% to be detected at the 95% confidence limit.

(2) The films used are clearly capable of recording more information than is conventionally done. The problem is that for higher

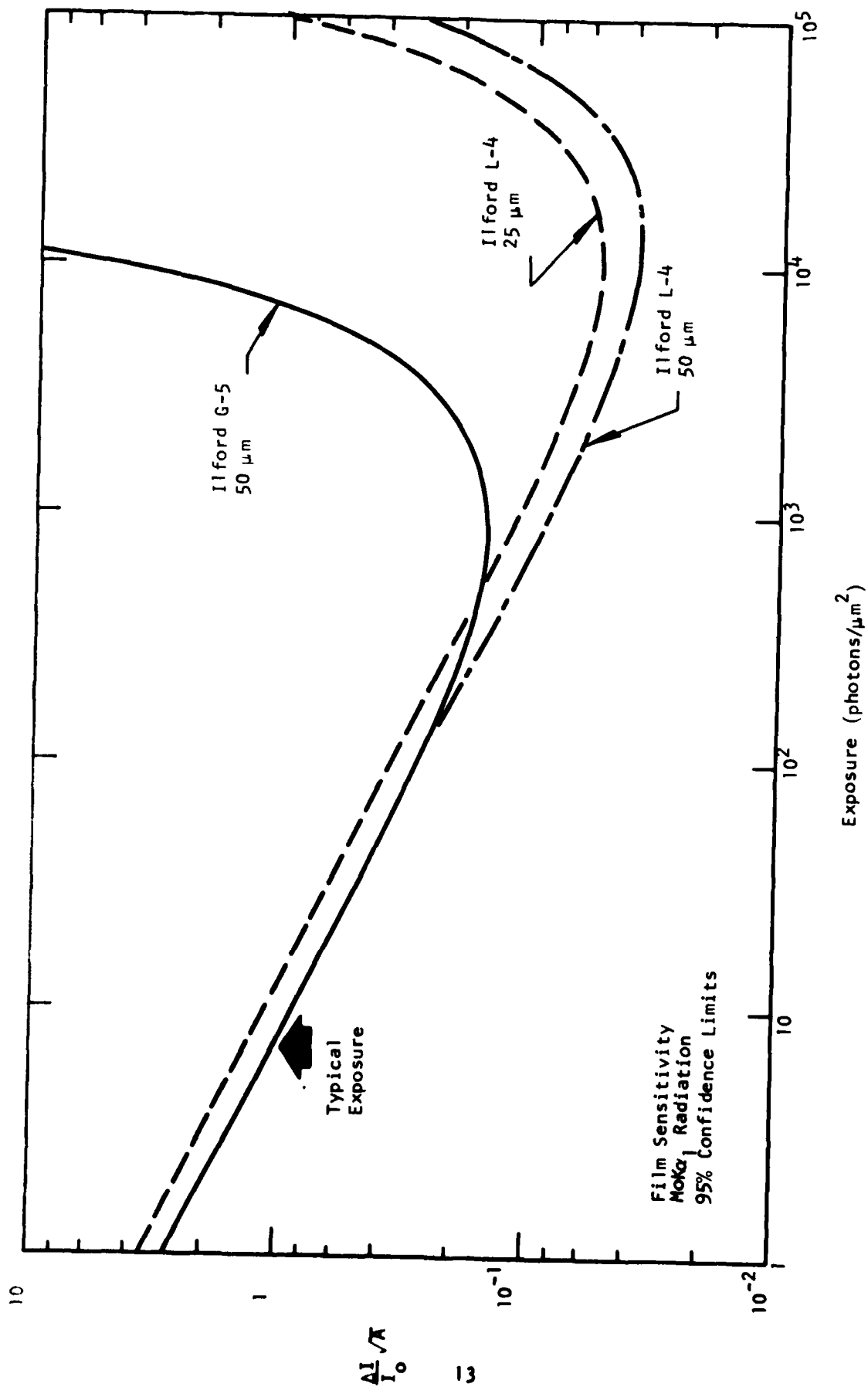


Figure 2(a) Film Contrast Sensitivity versus Exposure for  $\text{MoK}\alpha_1$  Radiation

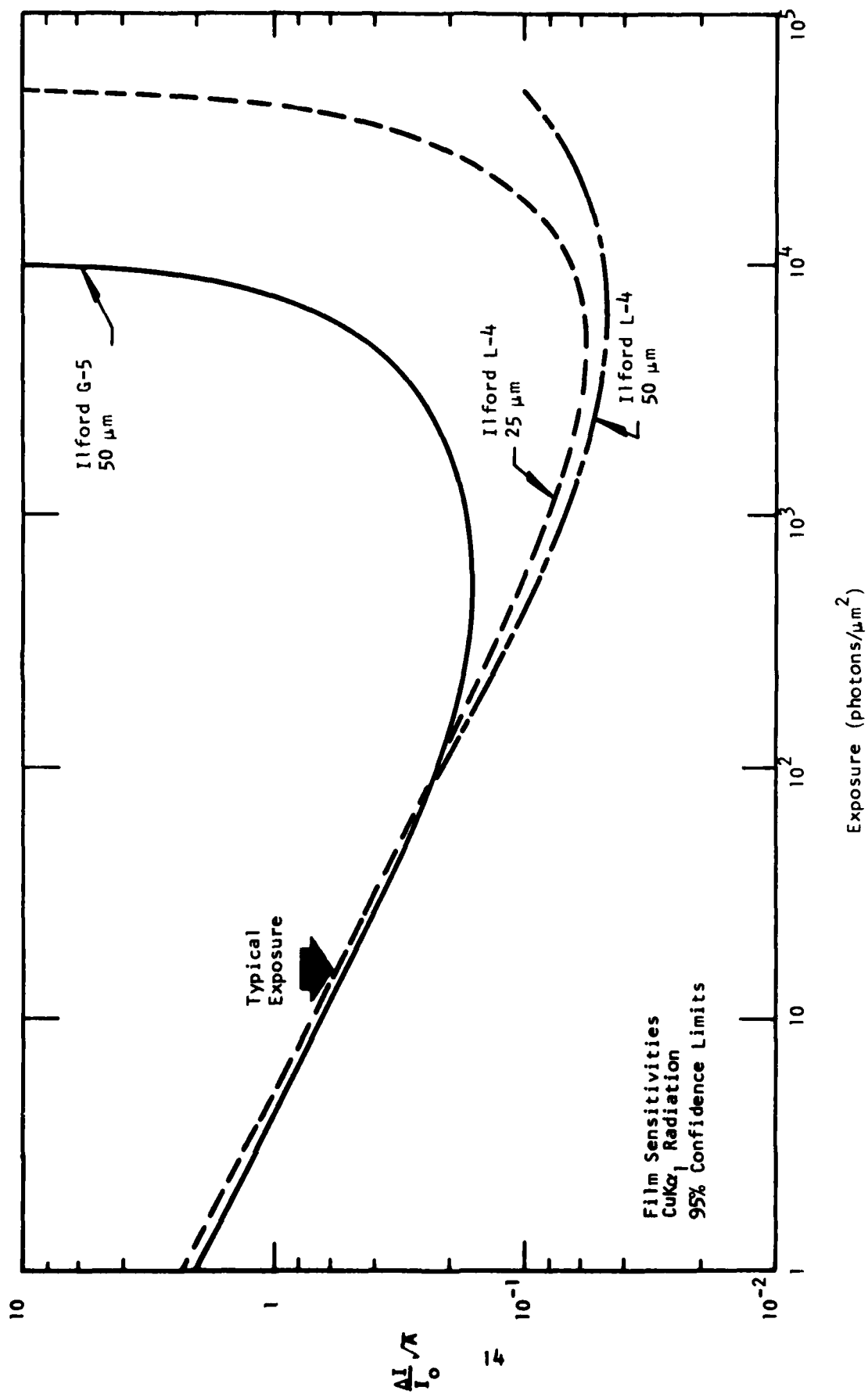


Figure 2(b) Film Contrast Sensitivity versus Exposure for CuK $\alpha_1$  Radiation



exposures, the film develops to solid black, and no detail can be seen. Mardix,<sup>14</sup> however, has shown that with conventional development and long exposures, defects can be seen that are invisible under conventional exposure by observing the surface relief caused by the tanning action of the developer. This confirms that the films are capable of recording considerably more information.

(3) Comparisons can be made between different experimental conditions in one of two ways. For a given exposure, a figure of merit can be calculated from:

$$\frac{\Delta I}{I_0} \sqrt{A} .$$

This will essentially correspond to using a given plate and photographic development for each topograph. Alternatively, and actually of more interest, we can assume that a developmental process can be adapted to a particular exposure, and that therefore the comparison is between topographs exposed for the same time. Under these circumstances the figure of merit will be:

$$\frac{\Delta I}{I_0} \sqrt{A t_0} .$$

(4) Because the graininess apparent in a topograph is a result of the statistical fluctuations of the x-ray quanta, development at low temperatures to suppress grain growth as is frequently done<sup>15</sup> makes no sense, since the developed grain size is less than 1  $\mu$ m in any event. The only advantage of such a development would be in suppressing film speed, which would require longer exposures.

Because of the enhanced sensitivity to defects offered by prolonged exposure, it is desirable to investigate whether unconventional techniques might allow the information to be developed from the film. Mardix's tanning

development<sup>14</sup> is such a technique, but suffers from resolution limitations, since tanning action results from the hardening of the gelatin caused by the products of development.<sup>13</sup> Since the exposed grains contributing to the picture element are located throughout the rather thick emulsion, the surface relief will not be strongly affected by deep-lying exposed grains. Shortened conventional development in an Elon-hydroquinone developer such as D-19 will also not be adequate because of the way in which these developers work. The characteristic of these developers is a rather slow incubation period of an exposed grain, followed by rapid silver filament growth.<sup>13</sup> Thus, a shortened development will result in a lower density due to the nondevelopment of grains, and hence to a loss of information.

Two developers reported in the literature may be applicable. The first, an Elon-ascorbic acid developer,<sup>16,17</sup> has been reported to give compact developed grains, and hence less optical density. The other, a developer based on para-phenylene diamine, has been reported to give extremely fine developed grains<sup>18,19</sup>; to develop all grains in parallel,<sup>20</sup> so that the final density can be adjusted by adjusting development time without loss of information; and to result in a significant decrease in film speed.<sup>21</sup>

#### 4. Conditions for Maximum Detectability

Combining the results of the previous sections, we come to the following result: that for the most sensitivity to defects in a given time, we want

$$\lambda \left( \frac{3}{2} - \frac{4}{n} \right) F(h) \left( \frac{3}{2} - \frac{2}{n} \right) \left( \frac{y_0}{y_h} \right)^{\left( \frac{1}{4} + \frac{1}{n} \right)} |h|^{-\frac{1}{2}}$$

to be as large as possible. We solve the above equation for the three defect types.

$$(1) \lambda^{-\frac{5}{2}} F(h)^{-\frac{1}{2}} \left( \frac{\gamma_o}{\gamma_h} \right)^{\frac{5}{4}} |h|^{-\frac{1}{2}}: \text{ dislocations}$$

$$(2) \lambda^{-\frac{1}{2}} F(h)^{-\frac{1}{2}} \left( \frac{\gamma_o}{\gamma_h} \right)^{\frac{3}{4}} |h|^{-\frac{1}{2}}: \text{ dislocation dipoles}$$

$$(3) \lambda^{\frac{1}{6}} F(h)^{\frac{5}{6}} \left( \frac{\gamma_o}{\gamma_h} \right)^{\frac{7}{12}} |h|^{\frac{1}{2}}: \text{ dislocation loops, precipitates.}$$

The computed values of these expressions are listed in Table 2, normalized to the largest value calculated. It should be noted that in this table comparisons should be made only vertically.

For the case of constant exposure, the following is a measure of sensitivity:

$$\lambda^{(1 - \frac{4}{n})} F(h)^{(1 - \frac{2}{n})} \left( \frac{\gamma_o}{\gamma_h} \right)^{\left( \frac{1}{2} + \frac{1}{n} \right)}.$$

Values of this function are listed in Table 3.

We have not yet considered the effect of the optical resolution. This can be rather drastic. For example, consider a defect with an image of  $1 \mu\text{m}$ . With a resolution of  $2 \mu\text{m}$ , the image on the plate will be about  $3 \mu\text{m}$ , and intensity will be reduced by a factor of 9. Thus, the detectability is reduced by a factor of 3. For a defect with an image size of  $5 \mu\text{m}$ , the reduction is only by a factor of 1.6.

Table 2  
Relative Sensitivity of Reflections to  
Detecting Defects (Constant Exposure Time)

Strain Field			$r^{-1}$	$r^{-2}$	$r^{-3}$	Size Independent
<u>Surface Normal</u>	<u>Radiation</u>	<u>Reflection</u>				
(111)	MoK $\alpha_1$ (Transmission)	11 $\bar{1}$	1.0	1.0	1.00	0.76
		2 $\bar{2}$ 0	0.74	0.85	0.89	0.76
		2 $\bar{2}$ 4	0.61	0.56	0.54	0.38
	CuK $\alpha_1$ (Reflection)	331	0.03	0.15	0.27	0.65
		224	0.03	0.21	0.39	1.00
		511	0.01	0.07	0.14	0.41
	MoK $\alpha_1$ (Transmission)	111*	1.0	1.0	1.00	0.76
		022	0.74	0.85	0.89	0.76
		040	0.65	0.47	0.67	0.52
(100)	CuK $\alpha_1$ (Reflection)	311*	0.01	0.06	0.13	0.61
		422	0.01	0.10	0.21	0.77
		511	0.05	0.21	0.32	0.58
	MoK $\alpha_1$ (Transmission)	400*	0.09	0.45	0.76	1.65

Note: All quantities normalized to highest sensitivity for strain field type.

\* Reflection for which film makes an angle greater than 30° with surface.  
Only limited resolution obtainable.

Table 3  
Relative Sensitivity of Reflections to  
Detecting Defects (Constant Exposure)

Strain Field			$r^{-1}$	$r^{-2}$	$r^{-3}$	Size Independent
Surface Normal	Radiation	Reflection				
(111)	MoK $\alpha_1$ (Transmission)	11 $\bar{1}$	0.89	1.00	0.95	0.77
		2 $\bar{2}$ 0	0.76	1.00	1.00	0.89
		2 $\bar{2}$ 4	1.00	1.00	0.91	0.68
	CuK $\alpha_1$ (Reflection)	331	0.02	0.15	0.26	0.63
		224	0.03	0.21	0.37	1.00
		511	0.01	0.07	0.13	0.39
	MoK $\alpha_1$ (Transmission)	111*	0.89	1.00	0.95	0.77
		022	0.76	1.00	1.00	0.89
		040	0.87	1.00	0.96	0.78
(100)	CuK $\alpha_1$ (Reflection)	311*	0.002	0.03	0.07	0.33
		422	0.006	0.07	0.27	0.59
		511	0.07	0.27	0.40	0.77
		400*	0.09	0.46	0.74	1.69

So far, we have considered defects whose image size is determined by the diffraction conditions. For a dislocation loop approximately  $1 \mu\text{m}$  in diameter, such as is found in swirl, the asymptotic limit has been described. However, close in to the dislocation, the material will diffract independently of the diffraction conditions, since it possesses a  $1/r$  strain field. For this case, we need to consider the quantity

$$\lambda^{\frac{3}{2}} |F(h)|^{\frac{3}{2}} \left( \frac{\gamma_o}{\gamma_h} \right)^{\frac{1}{4}} |h|^{\frac{1}{2}}$$

for the constant exposure time case, and

$$\lambda |F(h)| \left( \frac{\gamma_o}{\gamma_h} \right)^{\frac{1}{2}}$$

for the constant exposure case. The computed values of these expressions are also listed in Tables 2 and 3.

Concerning these tables, there are some general observations. First, the sensitivity in reflection topography is generally less than in transmission topography. This is primarily a result of the fact that the incident beam makes a small angle with the surface in the former case and hence  $\gamma_o/\gamma_h$  is small. In transmission topography, the reflection is generally symmetric, and hence  $\gamma_o/\gamma_h = 1$ . Second, the sensitivity of reflection topography to dislocations is particularly small in comparison to transmission topography. This is an additional result of the dependence of the image on wavelength -- the longer the wavelength, the smaller the defect image. Note that as the image dependence disappears, the sensitivity improves. Again, it should be emphasized that the sensitivities should be compared vertically only; dislocations are still very readily observed in reflection topographs.



Of the reflections listed, the (220) is obviously the most sensitive for transmission topography of both (100) and (111) slices under the usual conditions of constant exposure. For reflection topography, the (224) reflection for a (111) slice and the (511) reflection for a (100) slice are the best.

Under conditions of exposure for a constant time, assuming film speed can be appropriately adjusted, the (11 $\bar{1}$ ) reflection is superior for a (111) slice, while the (220) still remains best for a (100) slice for transmission topography. The (224) reflection for the (111) still remains the best in the reflection mode, while there is little difference in the quality of the (511) and the (422) reflections for a (100) slice. Clearly, the best way to look for swirl-type defects is with high efficiency reflections listed under the size independent column, and with long exposures.

The theory thus far developed clarifies a previous observation, namely that dark-current-producing defects are not always visible when the metal and oxide are still on the device. Two factors contribute to this phenomenon: since the strains from the metal and oxide cause a portion of the silicon to diffract kinematically, (1) if a defect is located within the region, it will contribute nothing to the image; and (2) if it is located outside this region, it will have to be seen on a much higher background, which greatly reduces the detectability.

#### B. Transmission Electron Microscopy

To achieve the goal of obtaining a 5000 Å thick region in a specified portion of an array bar, a multistep thinning procedure has been formulated. This procedure is as follows.

(1) The bar is ground to a thickness of 100 to 150 μm, while maintaining the ground surface parallel to the device surface to within ± 5 μm.

(2) The array is etched initially to 15 μm ± 10 μm. This will allow the nonplanarity of the etch to be ± 5 μm.

(3) A single 2.3 mm diameter disc is cut out in the desired region using a photoresist mask. The disc will be essentially planar and 5 to 25  $\mu\text{m}$  thick.

(4) The disc is given a final etch to thin it to 5000  $\text{\AA}$ .

(5) The disc is ion-milled, if necessary, to thin the desired region to 5000  $\text{\AA}$ .

To precisely locate the disc within the array, photographs will be taken after the disc is cut, but before it is dismounted from the remainder of the array.

### SECTION III

#### EXPERIMENTAL RESULTS

##### A. X-Ray Topography

The theoretical predictions of Section II have been previously confirmed for the case of a (111) slice under conditions of constant exposure. Based on the results of the (111) slice experimental work, we have been using a (422) reflection for reflection topography for a (100) slice. Because of the predictions of the previous section, we have undertaken an experimental evaluation of the (511) reflection for this slice orientation.

In anticipation of the need for long exposures for maximum sensitivity, the software on the Automated Topography System has been modified. The equipment is now capable of operating at scan speeds as slow as 0.0006 inch/minute (15  $\mu\text{m}/\text{minute}$ ). This will allow exposures to 670 photons/ $\mu\text{m}^2$ . A complete equipment shut-down sequence has also been programmed to allow overnight operation of the equipment.

The collimator tube of the x-ray camera is also being modified to allow the interior to be evacuated. This will increase the intensity of  $\text{CuK}\alpha$  x-rays by a factor of three.

Initial work on unconventional developers has begun. The Elon-ascorbic acid developer has no action on a plate (L-4) exposed directly in the x-ray beam. Since this is a surface developer,<sup>16</sup> it may be that an insufficient surface latent image is produced during x-ray exposure. Consequently, a predevelopment gold latensification<sup>17</sup> will be tried.

##### B. Transmission Electron Microscopy

Techniques for the new thinning procedure have been nearly completed. A summary of the work done and the results for each step of the procedure is given below.

### (1) Initial Grinding

Initial grinding is being done using a Buehler Whirlimet attachment. Problems were initially encountered with maintaining the surfaces parallel during grinding. This has been circumvented by the use of improved mounting techniques and an improved sample holder. The sample holder consists of three 1-inch diameter mounting blocks onto which the samples are mounted. These blocks are attached to a thick aluminum ring in such a way that the mounting blocks fit freely into the holes provided in the Whirlimet attachment. The surfaces of the mounting blocks are brought into flat relative to each other by grinding in the Whirlimet attachment through a 6  $\mu\text{m}$  diamond paste abrasive. Three bars to be ground ( $\sim 1\text{ cm} \times 1\text{ cm}$ ) are then placed on a glass plate with the side to be ground in contact with the plate, and spaced as they are to be mounted. Petroleum jelly is spread around the bars. The sample holder is heated on a hot plate, and black mounting wax is melted on each of the mounting blocks. The holder is then carefully lowered onto the samples and allowed to cool. When the wax has solidified, the sample holder is lifted, and excess wax and petroleum jelly are removed. The glass plate flat reference is maintained.

The samples and holder are then placed in the Whirlimet attachment and ground to the desired thickness using 600 grit silicon carbide paper. It has been determined that this procedure maintains the parallel between the two surfaces to within  $\pm 5\text{ }\mu\text{m}$  as the samples are ground from  $\sim 450\text{ }\mu\text{m}$  to  $\sim 100\text{ }\mu\text{m}$ .

Efforts to mount the sample directly using the polished or device side as reference have been totally unsuccessful.

The grinding rates are somewhat variable (from 5 to 10  $\mu\text{m}/\text{minute}$ ), probably because the sample holder does not ride freely within the Whirlimet jig.

## (2) Initial Etch

We have explored several possibilities in an effort to determine a suitable etch for the initial etch step. Two problems were encountered with many: (1) sensitivity to etch flow rate and (2) the tendency for the sample to pick up a surface film when it was removed from the etch, which irregularly inhibited etching when the sample was returned to the etch. In both cases, the result was a loss of surface planarity. An extreme example is shown in Figure 3, which shows a sample etched in three parts  $\text{HNO}_3$  to one part HF.

We have generally observed that etches containing a smaller volume fraction of HF and at least some acetic acid have etch rates less dependent on flow rate. Furthermore, we have found that samples etched in solutions containing  $\text{I}_2$  do not pick up a surface film and, consequently, resume etching readily. Therefore, we have settled on the following formula for the initial etch:

Solution A: 2.5 gms  $\text{I}_2$  dissolved in 550 ml acetic acid.

Solution B: 7 parts  $\text{HNO}_3$  to 1 part HF.

2 parts Solution B + 1 part Solution A.

Formulas similar to this have occasionally appeared in the literature,<sup>22,23</sup> although generally the  $\text{HNO}_3$ :HF ratio is 3:1.

The following etching procedure is used. The sample is mounted in the center of a stainless steel block 1 to 2 inches in diameter and 1/4 to 1/2 inch thick. The sample is placed in an inclined rotating beaker (~ 15 revolutions/minute) with 90 ml of the etch, such that the sample rotates by reason of its contact with the bottom beaker wall. After the appropriate etch, the sample is withdrawn from the etch and quenched with solution A. A cleanup using methanol then follows. Etch rates, unfortunately, are variable, in the range of 2.5 to 3.0  $\mu\text{m}/\text{minute}$ .

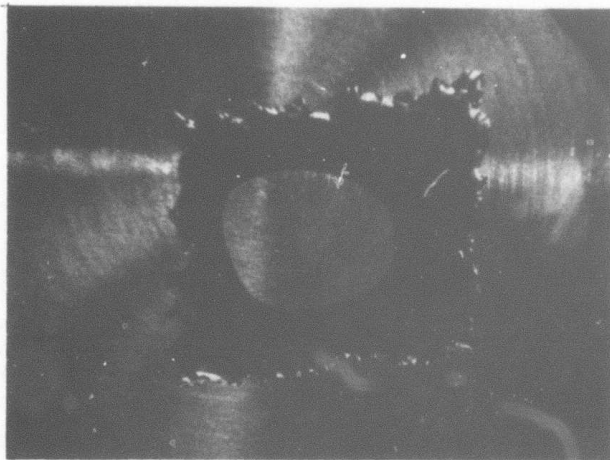


Figure 3 Silicon Bar Etched in 3 Parts  $\text{HNO}_3$  to 1 Part HF



With this etch we have successfully removed 100  $\mu\text{m}$  of silicon with a loss of planarity of only 5  $\mu\text{m}$ ; i.e., the sample was etched 5  $\mu\text{m}$  less at the edge than at the center.

### (3) Photoresist-Etch

We have made a photomask to cut out a single 2.3 mm diameter disc. Currently, a mounting attachment is being made to allow the irregularly shaped sample to be mounted in the photoresist spinner. It is anticipated that Kodak KMER photoresist will be used, followed by the urea:HF:HNO<sub>3</sub> etch of Kolbesen, et al.<sup>24</sup>

### (4) Final Etch

For the final etch, the disc is mounted on quartz glass using paraffin. Shoulders on the edge of the disc are defined by masking with paraffin. The sample is then etched by dipping into the same etch as before until the bright red stage appears. At this point an etch using a 20:1 HNO<sub>3</sub> to HF ratio as solution B is used. Etching continues until the bright yellow stage has appeared. This latter etch has an etch rate of approximately 0.8  $\mu\text{m}/\text{minute}$ . Quenching of the etch is done with solution A.

## C. Electrical Device Fabrication

### 1. Si Material Preparation

Study of electrically active defects in Si requires thorough knowledge of the growth and surface preparation of wafers used in the device fabrication tests. To explore the effects of variables involved in this process, three crystals were grown. Table 4 summarizes the specifications for subgroups of wafers from these crystals. In all cases, Varian Czochralski pullers were used. To maintain knowledge of the position of each wafer in the original crystal, a notch was cut diagonally along the flat before sawing. Examination of the notch in any given wafer will therefore reveal whether

Table 4  
Specifications for Subgroups of Wafers  
from Varian Czochralski Crystals

<u>Group #</u>	<u>Description</u>
1	<p>3 inch (7.62 cm) Varian Czochralski  Resistivity = 8 to 15 <math>\Omega</math> cm  Boron doped  Diameter = 2.985 to 3.010 inches (7.58 to 7.65 cm)  Orientation = 1-0-0 <math>\pm</math> 1°  Etch pit count &lt; 500  Lifetime &gt; 30 <math>\mu</math>sec  Flat orientation = 1-1-0 <math>\pm</math> 2°  Flat length = 0.9 to 1.1 inches (2.29 to 2.79 cm)  Notch in flat. Depth = 0.032 inch (0.081 cm)  Width = 0.115 to 0.135 inch  (0.292 to 0.343 cm)  Polished to 17 to 19 mils (0.43 to 0.48 mm)  Taper = 1.5 mils (0.038 mm)  Bow = 2.0 mils (0.051 mm)</p>
2	Same as 1, except backside abrasion added
3	<p>Same as 1, except  Flat orientation = 0-0-1 <math>\pm</math> 2°</p>
4	<p>Same as 1, except  Orientation = 1-1-1 <math>\pm</math> 1°  Flat orientation = 1-1-0 <math>\pm</math> 2°</p>
5	<p>Same as 1, except  Orientation = 1-1-1 <math>\pm</math> 1°  Flat orientation = 1-1-2 <math>\pm</math> 2°</p>
6	<p>Same as 1, except  Diameter = 1.985 to 2.010 inches (5.042 to 5.105 cm)  Orientation = 1-0-0 <math>\pm</math> 2°  Flat length = 0.5 to 0.6 inch (1.27 to 1.52 cm)  Bow = 1.5 mils (0.038 mm)</p>

the Si was near the seed or tail end of the original crystal. Varying wafer orientations will be useful both for x-ray topographic studies and for examination of defect propagation as a function of orientation of the active slip systems.

Crystals were ordered immediately after the beginning of the program, and the finished slices were received in October. Initial device fabrication and characterization tests were therefore performed on wafers that were already available. Although these wafers do not have notches for position identification, their resistivity, orientation, and quality specification were the same as those for Group #1.

## 2. Backside Damage Experiments

Reports of improved lifetime and "dislocation gettering" through use of backside-abrasion of Si slices<sup>25-27</sup> prompted examination of this material variable early in the program. Initial slices were prepared using a conventional sandblasting apparatus to abrade half of each 3 inch (7.62 cm) slice. In addition, #600 grit emery cloth was used to abrade half the backside area of other slices.

To supplement the CCD fabrication experiments on backside-damaged Si, a group of 2 inch (5 cm) slices was used to fabricate gate-controlled diodes. Glass beads 100  $\mu\text{m}$  in diameter were used to damage two slices on half of each backside area. Silicon carbide #600 grit paper was used in a spin swab apparatus to damage the entire back surface of two additional slices. Two slices were subjected to a heavy ( $5 \times 10^{16} \text{ cm}^{-2}$ , 150 kV) phosphorus implant in the backside before processing. Finally, two sandblasted slices and two undamaged slices were used for control purposes. Optical and SEM photographs of the back surface of all wafers were made after the damage process. Processing problems unrelated to the Si material were encountered with the first group of slices. A second group is now in process.

### 3. Device Fabrication

A > 80 K bit, two-phase CCD imaging array was chosen for material experiments in the program. The device had previously been designed for a TI program, and photomasks were readily available. The device structure is double-level polysilicon-aluminum, and the active array is  $0.86 \times 0.63 \text{ cm}^2$ .

Forty-five wafers were processed in the first lot, including 15 Varian-pulled Czochralski wafers, 15 wafers from a standard TI rf-heated Czochralski puller, and 15 Wacker float-zone slices. Devices that passed multiprobe tests were mounted on dual-in-line ceramic (CDIP) headers and characterized for image quality and total dark current. Results of the dark current measurements are shown in Table 5. Conversion of total dark current to  $\text{nA/cm}^2$  requires that figures in the table be multiplied by 1.85. Figure 4 shows placement of bars on a 3 inch (7.62 cm) wafer by device number.

Results of this experiment were surprisingly conclusive. Since all wafers were subjected to each processing step together and were randomly mixed in diffusion boats, differences among wafers can be considered to be largely a result of starting material. Examining dark current levels for any given wafer number reveals a statistically significant grouping. Although the number of devices tested is too small to be certain, it appears that a given starting wafer will tend to yield devices with dark current levels of the same order of magnitude if process variables are held constant.

A second result is also apparent from Table 5. The Wacker float-zone material yields a significantly higher level of dark current than either of the two types of Czochralski material. Comparison of the lowest dark current devices from each of the three groups gives 4.3 nA for rf-heated, 34.7 for Wacker float-zone, and 4.4 for Varian Czochralski. Corresponding average values are 51.0 nA, 76,881 nA, and 126.2 nA, respectively. Elimination of the worst Wacker wafer reduces that value to 90.24 nA, while the rf-pulled group would become 5.1 and the Varian, 20.2 nA.

Table 5  
Dark Current Measurements - Lot #1

<u>Wafer #</u>	<u>Device #</u>	<u>Material</u>	<u>Total Dark Current (nA)</u>
RF-9	27	RF-Heated Czochralski	4.3
RF-11	9		6.1
RF-11	26		5.0
RF-15	14		63.0
RF-15	20		138.0
RF-15	33	RF-Heated Czochralski	89.5
W-10	16	Wacker float-zone	153.7
W-10	22		29.8
W-11	5		14,600
W-11	9		250,000
W-11	23		350,000
W-12	17		150.0
W-13	21		34.7
W-13	22	Wacker float-zone	83.0
V-3	4	Varian Czochralski	56.3
V-3	6		55.8
V-3	33		71.8
V-4	10		19.2
V-4	28		5.9
V-4	34		7.0
V-13	21		5.2
V-13	27		5.1
V-13	29		13.3
V-14	27		4.4
V-15	4		815
V-15	5		280
V-15	26		168
V-15	32		619
V-16	21		5.8
V-16	22		8.5
V-16	27	Varian Czochralski	4.4

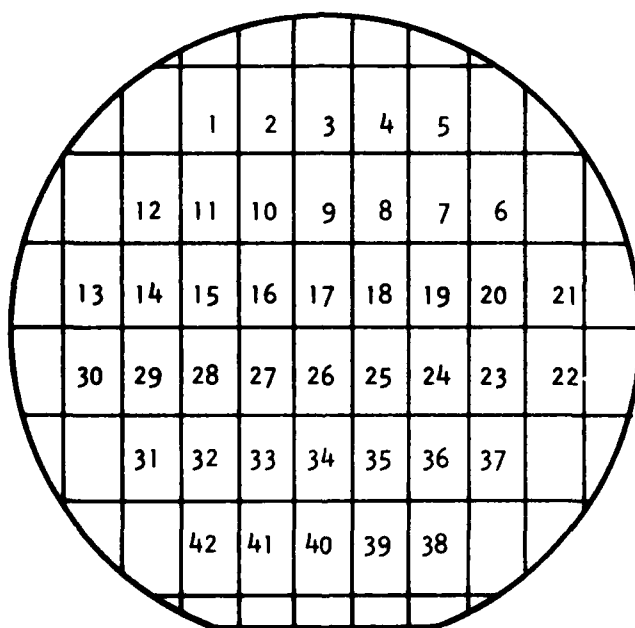


Figure 4 Device Number Positions on 7.6 cm Slices

Device dark current shows no clearly detectable trend with placement on the wafer, but the number of devices in this test is too small to attach meaning to this observation. Since devices from each of the three material groups appear to be randomly placed on the wafers, there is no reason to believe that placement affected the results seen in comparing the three groups.

Comparison of the float-zone results with Czochralski Si suggests that the reduced oxygen and carbon content achieved with float-zone techniques may not be the most important variable for controlling dark current. A possible explanation relates to the observation that the Wacker slices were heavily stress-relieved on the back surfaces. The two types of Czochralski material retained substantial backside damage from final grinding and therefore may have exhibited backside damage gettering.

A second experiment was conducted using three groups of silicon: (1) Varian Czochralski wafers with sandblasted back surfaces, (2) Shin-Etsu wafers with standard stress-relieved back surfaces, and (3) Varian Czochralski wafers with lightly stress-relieved back surfaces. Unfortunately, there were not enough good devices from this test to draw absolute conclusions, but there are some strong indications of material effects. Results are summarized in Table 6. The small number of Varian Czochralski wafers with sandblasted backsides do appear to show lower dark current levels than the same Varian slices without the backside damage. The Shin-Etsu silicon does not show significant improvement over standard Varian Czochralski Si, but is not significantly worse, either. Here again, the "near-polish" on the backside of the Shin-Etsu wafers (stress-relief) may be related to the device performance.

Completion of half-wafer backside damage tests should provide valuable additional information on this subject. Examination of individual dark current spikes, and the corresponding x-ray topographs, is expected to provide the most valuable data, especially when combined with in-process x-ray topographs that will show defect nucleation and propagation phenomena.

Table 6  
Dark Current Measurements - Lot #2

<u>Wafer #</u>	<u>Device #</u>	<u>Material</u>	<u>Total Dark Current (nA)</u>
V-6	9	Varian Czochralski - sandblasted	16
V-6	14	↓	23
V-6	34	Varian Czochralski - sandblasted	10
SE-7	2	Shin-Etsu	172
SE-7	4	↓	34
SE-7	6	↓	32
SE-7	15	↓	363
SE-7	25	↓	143
SE-7	27	↓	19
SE-7	32	↓	20
SE-7	38	↓	22
SE-7	39	Shin-Etsu	25
V-10	28	Varian Czochralski - standard backside	232
V-37	22	↓	28
V-37	30	↓	31
V-37	33	Varian Czochralski - standard backside	41



SECTION IV  
FUTURE RESEARCH

A. X-Ray Topography

Work on the high exposure processing of the topographic emulsion should continue, since it promises significant improvements in the sensitivity of topography to defects. While work has begun using conventional exposure techniques, it is hoped that work now under way will identify a developer that will allow the high exposure technique to be used.

B. Transmission Electron Microscopy

The problems of variable grinding rate and variable etch rates need to be brought under better control to reduce the time spent in monitoring these processes. It is anticipated that this may be accomplished while thinning of actual devices is taking place.

C. Device Fabrication and Testing

During the next quarter, the first lots of devices fabricated on the controlled material will be completed, and electrical and structural characterization of these devices will begin. In addition, in-process x-ray topography of a lot of material will be well under way. The results of these experiments are expected to shed considerable light on the nature and origin of dark-current defects as well as on the apparently beneficial nature of backside lattice damage in reducing dark current.

#### REFERENCES

1. H. F. Schaake, to be published.
2. Y. Ando, J. R. Potel, and N. Kato, J. Appl. Phys. 44, 4405 (1973).
3. N. Kato and J. R. Patel, J. Appl. Phys. 44, 965 (1973).
4. J. R. Patel and N. Kato, J. Appl. Phys. 44, 971 (1973).
5. B. C. Wonsiewicz and J. R. Patel, J. Appl. Crystallogr. 8, 67 (1975).
6. A. Authier, Phys. Status Solidi 27, 77 (1968).
7. A. Authier, Advanced in X-Ray Analysis 10, 9 (1967).
8. F. Meier, Z. Phys. 168, 10 (1962).
9. R. W. James, Solid State Phys. 15, 53 (1963).
10. R. W. James, The Optical Principles of the Diffraction of X-Rays (G. Bell and Sons, London, 1958), p. 41.
11. A. Authier, J. Phys. Radium 27, 57 (1966).
12. P. H. Dederichs, Solid State Phys. 27, 135 (1972).
13. T. H. James, ed., The Theory of the Photographic Process, (McMillan & Co., New York, 1966), 3rd ed.
14. S. Mardix, J. Appl. Phys. 45, 5103 (1974).
15. S. B. Austerman and J. B. Newkirk, Advances in X-Ray Analysis 10, 134 (1966).
16. J. F. Hamilton and L. E. Brady, J. Appl. Phys. 30, 1893 (1959).
17. M. M. Salpeter and L. Bachmann, J. Cell Biology 22, 469 (1964).
18. L. G. Caro and R. P. Tubergen, J. Cell Biology 15, 173 (1962).
19. T. H. James in The Theory of the Photographic Process, (McMillan & Co., New York, 1966) 3rd ed., p. 324.
20. H. Arens and J. Eggert, Z. Elektrochem. 30, 49 (1929).

21. C. B. Nebletts, Photography, Its Materials and Processes, (van Nostrand, New York, 1962), p. 233.
22. J. E. Lawrence and H. Koehler, J. Sci. Instrum. 42, 270 (1965).
23. W. Wu and J. Washburn, J. Appl. Phys. 45, 1085 (1974).
24. B. O. Kolbesen, K. R. Mayer, and G. E. Shuh, J. Phys. E. 8, 197 (1975).
25. J. E. Lawrence, "Method of Preparing High Yield Semiconductor Wafer," U. S. Patent #3,905,162, September 16, 1975.
26. R. G. Herring, "Suppression of Oxidation Induced Stacking Faults in Silicon," Electronic Materials Conference, Salt Lake City, Utah, May 1976.
27. G. Schwuttke, Private Communication.